Exploring the sky localization and early warning capabilities of third generation gravitational wave detectors in three-detector network configurations

Yufeng Li[1,2,3] Ik Siong Heng[3,*] Man Leong Chan,[4] Chris Messenger,[3] and Xilong Fan[5]

[1]*Key Laboratory for Computational Astrophysics, National Astronomical Observatories, Chinese Academy of Sciences, Beijing 100101, China*
[2]*School of Astronomy and Space Science, University of Chinese Academy of Sciences, Beijing 100049, China*
[3]*SUPA, School of Physics and Astronomy, University of Glasgow, Glasgow G12 8QQ, United Kingdom*
[4]*Department of Applied Physics, Fukuoka University, Nanakuma 8-19-1, Fukuoka 814-0180, Japan*
[5]*School of Physics and Technology, Wuhan University, Wuhan 430072, China*

This work characterizes the sky localization and early warning performance of different networks of third generation gravitational wave detectors, consisting of different combinations of detectors with either the Einstein Telescope or Cosmic Explorer configuration in sites in North America, Europe, and Australia. Using a Fisher matrix method which includes the effect of earth rotation, we estimate the sky localization uncertainty for 1.4 $M_\odot$–1.4 $M_\odot$ binary neutron star mergers at distances 40, 200, 400, 800, and 1600 Mpc, to characterize each network's performance for binary neutron star observations at a given distance. We also characterize each network's sky localization capability for an assumed astrophysical population up to redshift ≤ 2. Furthermore, we also study the capabilities for the different networks to localize a binary neutron star merger prior to merger (early warning) and characterize the network performance for sky localization uncertainty between 1 and 30 square degrees. We find that, for example, for binary neutron star mergers at 200 Mpc and a network consisting of the Einstein Telescope, Cosmic Explorer, and an extra Einstein Telescope-like detector in Australia (2ET1CE), the upper limit of the size of the 90% credible region for the best localized 90% signals is 0.25 deg^2. For the simulated astrophysical distribution this upper limit is 91.79 deg^2. If the Einstein Telescope-like detector in Australia is replaced with a Cosmic Explorer-like detector (1ET2CE), for signals at 200 Mpc, the size of the 90% credible region for the best localized 90% signals is 0.18 deg^2, while the corresponding value for the best localized 90% sources following the astrophysical distribution is 56.77 deg^2. We note that the 1ET2CE network can detect 7.2% more of the simulated astrophysical population than the 2ET1CE network. In terms of early warning performance (e.g., 200 Mpc), we find that a network of 2ET1CE and 1ET2CE networks can both provide early warnings of the order of one hour prior to merger with sky localization uncertainties of 30 square degrees or less. In some cases, the 2ET1CE network is capable of estimating the sky location with an uncertainty of five square degrees or less on timescales of about one hour prior to merger. Our study concludes that the 1ET2CE network is a good compromise between binary neutron stars detection rate, sky localization, and early warning capabilities.

I. INTRODUCTION

The first directly detected gravitational wave (GW) event GW150914 by Advanced LIGO in September 2015 opened a new window on exploring the Universe [1]. During the first two observation runs (O1 and O2) of Advanced LIGO, and Advanced Virgo (joined in O2) [2], a total of ten binary black holes (BBHs) mergers and one binary neutron star

(BNS) merger were identified [3]. The follow-up observations of the electromagnetic (EM) counterparts of the BNS event have initiated the GW and EM multimessenger astronomy era [4]. In 2019, the Advanced LIGO and Advanced Virgo started the third observation run (O3) with improved sensitivities. O3 has finished and 39 GW candidates from the first half of O3 have been released in 2020 as the second Gravitational-Wave Transient Catalog (GWTC-2) [5]. More recently, a deeper list of candidate events over the same period of GWTC-2 was reported recently in the LIGO Scientific Collaboration *et al.* [6] as

*Corresponding author.
ik.heng@glasgow.ac.uk

GWTC-2.1, which revealed 44 high-significance candidates. It is expected that a large number of GW events will come into our view with the improvement in sensitivity of the upcoming fourth observation run and more distant third generation detector era.

In the frequency band relevant to ground based GW detectors, the most common sources of GW events are expected to be compact binary coalescences (CBCs).

In addition to the exploration of the source properties for a single CBC system, GW detections could also shed light on the merger rate of CBC systems as a function of distance from us, thus test theoretical models for the CBC merger rate and give further clues to the studies of formation of single CBC systems. For example, the BNS merger rate is constrained to be 1540^{+3200}_{-1220} Gpc^{-3} yr^{-1} by the detection of GW170817 [4], and the latest BNS merger rate is found to be 320^{+490}_{-240} Gpc^{-3} yr^{-1} by the second LIGO-Virgo Gravitational-Wave Transient Catalog [7]. Beyond that, a fundamental method to estimate merger rate distribution, delay time distribution (DTD), attracts some attempts to evaluate its validity by current second generation GW detectors and future third generation GW detectors [8–10]. As explored in a series of researches not limited to Hachisu *et al.* [11], Piran [12], Safarzadeh and Berger [8], Safarzadeh *et al.* [9,10], and Zheng and Ramirez-Ruiz [13], the merger rate distribution is a convolution of the cosmic star formation rate and the distribution of delay time distribution between the system form and merger. Specifically, the DTD is usually parametrized as a power law distribution with a slope Γ above minimum merger timescale t_{min}. In a later analysis, we generate GW sources following DTD to simulate a realistic distribution in the Universe.

Systems of CBCs which include at least one neutron star, such as the mergers of BNS or neutron star black hole (NSBH), are likely to generate observable EM emissions. These emissions include short-duration gamma-ray bursts (SGRBs), powered by accretion onto the central compact object [14], and an isotropic thermal emission powered by the radioactive decay of heavy elements in the merger ejecta, known as kilonova [15], as well as optical and radio afterglows [16]. Successful EM follow-up observations of a GW event can identify the host galaxy, and provide information on the progenitor local environment and the hydrodynamics of the merger [17–19]. Coupled with the estimates of a model-independent luminosity distance derived from GWs, it is even possible to infer the values of the Hubble constant [20–22]. In terms of EM follow-up observations, the most needed information from GWs is the estimate of the sky location of the source, the size of the error region, and the time at merger. To increase the likelihood of successful EM follow-up observations improvement in localization of GWs is desired. On the other hand, if the in-band duration of a GW signal is long enough that its presence can be identified and information

on its sky location obtained well before the merger, astronomers will be allowed more time to prepare, further increasing the likelihood of successful EM follow-up observations. This is known as early warning [23]. For BNSs, the in-band duration of a signal mainly depends on the low cut-off frequency of GW detectors and the masses of the systems. For example, the in-band duration of the inspiral signal of a $1.4\ M_\odot - 1.4\ M_\odot$ BNS meger in a GW detector with a low cutoff frequency of 10 Hz is $\mathcal{O}(10^3)$ s.

Third generation GW detectors such as the Einstein Telescope (ET) [24] and the Cosmic Explorer (CE) [25] are expected to be built in the 2030s. With sensitivities better than that of the second generation detectors, observing GWs from BBH and BNS sources located at distances far greater than the horizon of second generation detectors will be possible, thus could contribute to explorations of compact object evolution so as to further study the evolution of the Universe. Localization of CBC sources detectable by the second generation detectors and CBC sources at greater distances could also benefit from improved sensitivity of the third generation detectors due to higher SN ratio, and the improved sensitivity of third generation GW detectors at low frequency band, for example, 1 Hz–10 Hz, allows for a longer in-band duration (e.g., low cutoff frequency 1 Hz, in-band duration will be five days) for CBC signals as the time to merger is inversely related to the instantaneous GW frequency (which we will introduce later) thus jointly leading to promising EM follow-up observations as stated in previous researches such as Akcay [26], Akcay *et al.* [27], Chan *et al.* [28], Mills *et al.* [29], and Zhao and Wen [30]. It should be noted that we consider the Earth's rotation due to the long duration of simulated signals.

In this paper, using a Fisher matrix approach, we estimate the localization uncertainty and early warning prospect for networks of third generation ground-based GW detectors for BNSs. We simulate BNS mergers at fixed distances as well as a population following the DTD of a power law distribution with a slope $\Gamma = -1.5$ and a minimum merger time $t_{\mathrm{min}} = 1$ Gyr.

Previous studies have shown the benefits of building a detector in Australia because of the long baseline that such a detector will form with other detectors [31–33]. This paper aims to characterize the performance of a network of three third generation detectors which consists of different permutations of detectors in CE and ET configurations. Thus, in addition to the proposed third generation GW detectors, the ET and CE, we assume an ET-like detector or a CE-like detector in Australia.

This paper is arranged as follows. In Sec. II, the basic information of the third generation detectors are introduced. In Sec. III, we present the information of sources in simulations and explain the Fisher matrix method used to estimate the localization errors. The results of the simulations are discussed in Sec. IV. Finally, in Sec. V, a discussion and a conclusion are provided.

II. THIRD GENERATION DETECTORS

Third generation GW detectors aim to improve the sensitivity across the entire frequency band. [25,34]. At present, the two proposed third generation detectors are the ET and the CE. The ET is composed of three interferometers with 10 km long arms. The interferometers will each have an opening angle equal to 60° and each of them will be rotated relative to the others by 120°, forming an equilateral triangular structure. Proposed locations for the ET include Sardinia, Italy, and the border region between the Netherlands, Belgium, and Germany. The target sensitivity of the ET is shown in Fig. 1. For frequency larger than 10 Hz, compared to the Advanced LIGO and Advanced Virgo, the sensitivity of the ET will be improved by a factor of ~10, and even better for frequencies below 10 Hz. A detailed description of the ET can be found in Punturo et al. [24,34].

Unlike the ET, the CE will have the typical L-shaped configuration employed by second generation detectors, with an arm length of 40 km. For frequencies ≥10 Hz, as shown in Fig. 1, the sensitivity is improved by a factor of ~30 compared to Advanced LIGO and Advanced Virgo [25,35]. The planned location for the CE is North America. More extensive technology details about the CE can be found in Reitze et al. [36].

With the improvement of sensitivity, the ET is expected to be able to detect mergers of BNS at redshifts of about 2, and it will be even higher for CE [37]. On the one hand, the improved sensitivity of GW detectors at frequencies ≥10 Hz will directly lead to a higher signal-to-noise (SN) ratio so as to improve the localization of GW events. On the other hand, the improved sensitivity for the frequency band of 1 Hz–10 Hz will greatly extend the in-band duration of GW signals, so as to improve the localization as shown in [28,37].

Assuming the detector is at the center or a spherical coordinate system, the antenna pattern of each interferometer of an ET-like detector can be expressed as follows [38]:
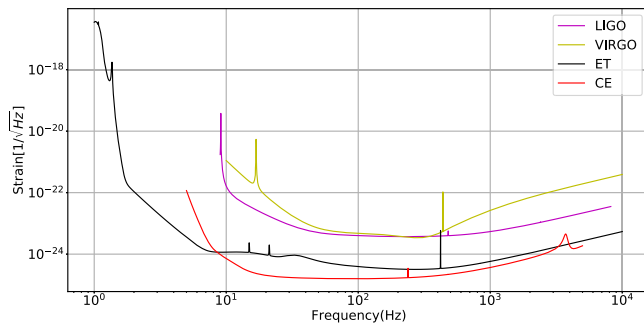

FIG. 1. The sensitivity curve of the second generation detectors LIGO, Virgo, and the third generation detectors ET and CE.

$$F_+^1(\theta, \phi, \psi) = -\frac{\sqrt{3}}{4}[(1 + \cos^2\theta)\sin 2\phi \cos 2\psi$$
$$+ 2\cos\theta \cos 2\phi \sin 2\psi],$$

$$F_\times^1(\theta, \phi, \psi) = \frac{\sqrt{3}}{4}[(1 + \cos^2\theta)\sin 2\phi \sin 2\psi$$
$$- 2\cos\theta \cos 2\phi \cos 2\psi],$$

$$F_{+,\times}^2(\theta, \phi, \psi) = F_{+,\times}^1\left(\theta, \phi + \frac{2\pi}{3}, \psi\right),$$

$$F_{+,\times}^3(\theta, \phi, \psi) = F_{+,\times}^1\left(\theta, \phi - \frac{2\pi}{3}, \psi\right), \qquad (1)$$

where F_+^n is the plus polarization response of the nth interferometer and $F_\times^n$ is the cross polarization response. The antenna patterns are a function of the azimuthal angle θ, the polar angle ϕ and the polarization angle ψ, of the GW source. The antenna pattern of the CE can be expressed as [39]

$$F_+(\theta, \phi, \psi) = \frac{1}{2}(1 + \cos^2\theta)\cos 2\phi \cos 2\psi$$
$$- \cos\theta \sin 2\phi \sin 2\psi,$$

$$F_\times(\theta, \phi, \psi) = -\frac{1}{2}(1 + \cos^2\theta)\cos 2\phi \sin 2\psi$$
$$- \cos\theta \sin 2\phi \cos 2\psi. \qquad (2)$$

where, as before, F_+ is the plus polarization response for CE and $F_\times$ is the cross-polarization response. In addition, better sensitivity of a detector such as the ET in the low-frequency band enables longer in-band signal duration; generally, 1 Hz corresponds to about five days as explained in Sec. III. Therefore, the azimuthal angle and polar angle will change over time as the Earth keeps rotating, which means the antenna pattern will also be time dependent. Additionally, due to the long duration of signal, the signal will experience the Doppler effect because the detector moves relative to the signal, in terms of the Doppler effect, Chan et al. [28] suggests that the Doppler effect is not important to the localization uncertainty estimation, while for completeness, we also included the Doppler effect in our analysis.

For our study, we assume that the ET is located at the Virgo site in Italy (longitude, latitude) = (10.4 °E, 43.7 °N), and the CE at the LIGO Hanford site in the United States (longitude −119.41 °E, latitude 46.45 °N). Though it is likely that the final locations of the CE and the ET will not be at these assumed locations, the impact of any change in location within the United States and Europe will be small since our study is looking at the results averaged across a population of simulated signals. Additionally, we consider a third detector located in Australia (longitude 115.87 °E, latitude −31.95 °N) for our study. Specifically, we assume two different scenarios. In the first scenario, the detector

TABLE I. The simulated GW detector networks in this paper. The first row is the locations of the GW detectors in longitude and latitude. The left column shows the names of the GW detector networks, which directly indicates the network configuration. ET-A and ET-L represent an ET-like detector in Australia and the LIGO Hanford site respectively. Similarly, CE-A and CE-V indicate a CE-like detector located in Australia and Italy.

	Australia (115.87 °E, −31.95 °N)	LIGO Hanford (−119.41 °E, 46.45 °N)	Italy (10.4 °E, 43.7 °N)
2ET1CE	ET-A	CE	ET
3ET	ET-A	ET-L	ET
1ET2CE	CE-A	CE	ET
3CE	CE-A	CE	CE-V

located in Australia is a detector with sensitivity and configuration identical to those of the ET, denoted by ET-A, while in the other scenario, the detector will be similar to CE, referred to as CE-A. To further explore the localization capabilities of different combinations of third generation GW detectors, two detectors, denoted by ET-L and CE-V, are introduced. Similarly, ET-L indicates an ET-like detector at the location of LIGO Hanford, and CE-V refers to a CE-like detector at the Virgo site.

We simulate four networks of GW detectors. The simulated networks can be found in Table I. We use the numbers and the types of the detectors in a network to refer to the network. For example, 2ET1CE refers to a network consisting of two ET-like detectors and one CE-like detector, and 3ET to a network consisting of three ET-like detectors. We estimate the localization uncertainty and the prospect for early warning for these networks.

III. METHODOLOGY

A. Binary neutron star simulations

Generally, the evolution of BNSs is considered to go through three stages; inspiral, merger, and ringdown. The GW signal during the adiabatic inspiral phase can be well described by post-Newtonian [40]. Our major goal is the localization performance achieved before the merger of BNSs to evaluate early warning capabilities; thus, our demand for an accurate description of the merger and ringdown is not high. In this context, the strain of an incoming GW observed at the dth interferometer can be expressed as $h_d(\boldsymbol{\theta}, t)$, which is a linear combination of the two polarizations of the wave $h_+(\boldsymbol{\theta}, t)$ and $h_\times(\boldsymbol{\theta}, t)$, as well as the response of the interferometer, i.e., $h_d(\boldsymbol{\theta}, t) = F_+(\theta, \phi, \psi)h_+(\boldsymbol{\theta}, t) + F_\times(\theta, \phi, \psi)h_\times(\boldsymbol{\theta}, t)$. $\boldsymbol{\theta}$ is a vector representing the parameters of the wave defined in Sec. III B. In this work, the two polarizations of a signal $h_+(\boldsymbol{\theta}, t)$ and $h_\times(\boldsymbol{\theta}, t)$ are approximated using the TaylorT3 waveform (specifically, Eq. (3.10b) in [41]) approximant.

In addition to the signal templates, the duration of simulated signals also need to be taken into consideration. The duration of simulated signal, in other words, the time remaining to merger, can be simply estimated according to a leading-order post-Newtonian approximation as follows [42]:

$$\tau_c = \frac{5}{256}\frac{c^5}{G^{\frac{5}{3}}}\frac{(\pi f_s)^{-\frac{8}{3}}}{\mathcal{M}^{\frac{5}{3}}},\qquad(3)$$

where τ_c is the time to merger, c the speed of light, G the gravitational constant, $\mathcal{M}$ the chirp mass ($\mathcal{M} = \frac{(m_1 m_2)^{3/5}}{(m_1+m_2)^{1/5}}$, where $m1, m2$ are component masses), and f_s the low cutoff frequency. It should be noted that component masses, chirp masses, and total masses ($M = m_1 + m_2$) in our simulations are all redshifted to the observed mass M_{obs} by

$$M_{obs} = M_{local}(1+z).\qquad(4)$$

Now assuming a low cutoff frequency of 1 Hz and a BNS of 1.4 $M_\odot$–1.4 $M_\odot$, the in-band duration of the GW signal can be estimated to be about 130 hours. Naturally, during detection for signals with a duration of 130 hours, the Earth keeps rotating—in this context a time-dependent antenna pattern needs to be applied for a reliable estimation for localization.

To estimate the localization for different populations of BNS mergers, two scenarios are considered, BNSs at fixed distances, and a population of BNSs with a redshift distribution following the power law DTD described in Safarzadeh *et al.* [9]. For BNSs at fixed distances, we select 40, 200, 400, 800, and 1600 Mpc as examples. Specifically, 100 BNSs are simulated for each distance. 500 BNSs sources following the DTD of redshift up to two are simulated.

The mass of the simulated BNSs are all 1.4 $M_\odot$–1.4 $M_\odot$ in local frame. The sky locations (the right ascension α and declination δ) of the simulated BNS mergers for all cases are randomly sampled to simulate uniform distribution in the whole sky. The cosine of inclination angle $\cos\iota$ are randomized in the range between −1 and 1 and the polarization angle ψ is also randomized in range between 0 and 2π.

For the BNS mergers following the DTD used in this work, the BNS merger rate as a function of redshift z can be expressed as

$$R(z) = \int_{z_b=10}^{z_b=z} \lambda \frac{dP_m}{dt}(t - t_b - t_{min})\text{SFR}(z_b)\frac{dt}{dz}(z_b)dz_b.\qquad(5)$$

Here, $R(z)$ represents the BNS intrinsic merger rate density (Mpc^{-3} year^{-1}), and SFR represents cosmic star formation rate density ($M_\odot$ yr^{-1} Mpc^{-3}). λ is the BNS mass efficiency

which is assumed to be a constant $10^{-5} \, M_\odot^{-1}$, t_b is the time at the redshift z_b, and dP_m/dt is the DTD which is assumed to follow a power law distribution with a minimum delay time, and Γ as the power law index, given by

$$dP_m/dt \propto t^\Gamma, \qquad (6)$$

and $t_{\min}$ in Eq. (5) is the minimum delay time which corresponds to the time since the star first joins the main sequence on the Hertzsprung-Russell diagram. In this paper, we adopt $t_{\min} = 1$ Gyr and $\Gamma = -1.5$. The derivative of time, dt/dz, with respect to redshift is given by

$$dt/dz = -[(1+z)E(z)H_0]^{-1}, \qquad (7)$$

where

$$E(z) = \sqrt{\Omega_{m,0}(1+z)^3 + \Omega_{k,0}(1+z)^2 + \Omega_\Lambda(z)}, \qquad (8)$$

where Ω_M is the matter density, Ω_Λ vacuum density, Ω_K curvature, and H_0 the Hubble constant. We adopt the values from the Planck 2015 results [43]. In particular, $\Omega_M = 0.308$, $\Omega_\Lambda = 0.692$, $\Omega_K = 0$, and $H_0 = 67.8 \text{ km s}^{-1} \text{ Mpc}^{-1}$ respectively. For the cosmic star formation rate density SFR(z), we adopted the following formula from [9,44]

$$\text{SFR}(z) = 0.015 \frac{(1+z)^{2.7}}{1 + [(1+z)/2.9]^{5.6}} \, M_\odot \, \text{yr}^{-1} \, \text{Mpc}^{-3}, \qquad (9)$$

where z represents the redshift. In Eq. (5) we chose the lower limit of integration to be redshift of 10 based on Safarzadeh et al. [9], because the choice of maximum redshift has little impact on the calculation. In the case of $t_{\min} = 1$ Gyr, $\Gamma = -1.5$, we calculated its corresponding BNS merger rate density for a redshift range from 0 to 2 via Eq. (5). And by assuming the integral of BNS merger rate density over redshift range from 0 to 2 is 1 (that is, all sources are distributed within redshift range of 0–2), the redshift distribution (namely, the probability density function of redshift) of sources could be obtained as shown in Fig. 2. We simply chose two as the maximum redshift cutoff.

B. Fisher matrix analysis

The Fisher matrix translates errors on observed quantities measured directly into constraints on parameters of interest in the underlying model [45], which has been tested as an applicable tool in a series of research [28–30,46–48] to estimate localization errors for GW detectors with lower computation cost compared to other methods. As elaborated in Vallisneri [49], the inverse Fisher matrix represents the covariance matrix of parameter errors for the true signal, which could also be interpreted as the frequentist error covariance for the maximum-likelihood parameter estimator assuming Gaussian noise in the case of high SN
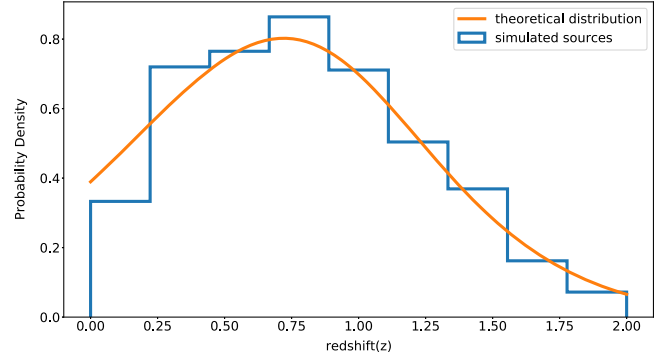

FIG. 2. The redshift distribution of simulated sources. The x-axis represents the redshift. The y-axis represents the normalized distribution which makes the area under the curve is 1. The orange line is the redshift distribution calculated using Eq. (5) with $t_{\min} = 1$ Gyr, $\Gamma = -1.5$, and the blue line is the distribution of simulated sources.

ratio limit (that means, the waveforms could be considered as linear functions of source parameters). And in the high SN ratio limit, the maximum-likelihood naturally achieves the Cramér-Rao bound. Therefore that's why we set a SN ratio threshold for further localization uncertainty analysis. Only those signals detected with a SN ratio larger than or equal to the SN ratio threshold are seen as detectable signals. In this paper, we chose a network SN ratio of 8 as the detectable threshold. In addition, for waveforms of low SN ratio or waveforms with poor priors estimation for its parameters, the Fisher matrix could not be applied to parameter estimation of GW data credibly. Also, it is worth noting that the detector network consisting of three detectors significantly improves the sky localization accuracy compared to two-detector networks and thus enhances the reliability to estimate localization error via the Fisher matrix method [50].

We consider a vector, $\boldsymbol{\theta}$, of nine parameters in our Fisher matrix analysis as in Chan et al. [28]; α, δ, the arrival time of the signal at the center of the Earth t_0, the log of distance $\log_{10} d$, the polarization angle ψ, the log of the total mass $\log_{10} M$, the cosine of the inclination angle $\cos \iota$, the symmetric mass ratio $\eta = m_1 \times m_2/M^2$, and the initial phase of the wave when it arrives at the center of the earth ϕ_0. The elements of $\boldsymbol{\theta}$ in the Fisher matrix then could be obtained by

$$\text{FIM}_{ij} = \sum_{d=1}^{N} 2 \int_0^\infty \frac{\frac{\partial h_d^*}{\partial \theta_i} \frac{\partial h_d}{\partial \theta_j} + \frac{\partial h_d^*}{\partial \theta_j} \frac{\partial h_d}{\partial \theta_i}}{P_d} \, df, \qquad (10)$$

where h_d, obtained by converting $h_d(\boldsymbol{\theta}, t)$ to the frequency domain using Fourier transform, represents the incoming gravitational wave strain in the frequency domain at the dth detector $\frac{\partial h_d}{\partial \theta_i}$ denotes the partial derivative of h_d with respect to the ith unknown parameter θ_i. P_d refers to the power

spectral density for the dth interferometer. The optimal SNR, $\rho_{\rm d}$, for the dth detector can be expressed as

$$\rho_{\rm d} = \sqrt{4 \int_0^\infty \frac{|h_{\rm d}(\boldsymbol{\theta}, f)|^2}{P_{\rm d}(f)} df}. \tag{11}$$

The combined SNR for a signal from a network of detectors can be obtained by

$$\rho_{\rm network} = \sqrt{\sum_{\rm d=1}^N \rho_{\rm d}^2}. \tag{12}$$

In simulation, we divide the strain data in the time domain into S segments with length of 100 sec (the last segment shorter than 100 sec), and use Eq. (10) to calculate the Fisher matrix for each segment. The Doppler effect is also taken into account by considering that the time delays between the center of the Earth and each interferometer are a function of time and change as the Earth rotates. The Fisher matrix for the entire signal is then obtained by summing the Fisher matrices over the segments,

$$\text{FIM}_{ij}^t = \sum_{k=1}^S \text{FIM}_{ij}^k, \tag{13}$$

where t represents variable for the entire signal, and k indicates the kth segment. The total accumulated SN ratio of single detector for the entire signal ρ_d^t is obtained by

$$\rho_d^{\rm t} = \sqrt{\sum_{k=1}^S (\rho_d^k)^2}, \tag{14}$$

where ρ_d^k represents the SN ratio of kth segment for dth detector. The covariance matrix can then be derived by computing the inverse of the Fisher matrix,

$$\text{cov}_{ij}^t = (\text{FIM}_{ij}^t)^{-1}. \tag{15}$$

From the nine dimensional cov_{ij}^t, a two-dimensional covariance matrix $\text{cov}_{\alpha\delta}$ corresponding to α and δ is extracted. The localization uncertainty $\Delta\Omega$ is then given by

$$\Delta\Omega = \pi \sqrt{\lambda_\alpha \lambda_\delta} \cos \delta, \tag{16}$$

where λ_α and λ_δ are the eigenvalues of $\text{cov}_{\alpha\delta}$. Finally, the localization uncertainty at confidence level p is obtained by [51]

$$\Delta\Omega_p = -2 \log(1-p)\Delta\Omega. \tag{17}$$

IV. RESULTS

We use a network SN ratio of 8 to determine whether an event is detectable. To avoid ambiguity, the localization errors shown in the remaining of this paper are all at 90% confidence level.

A. Sources at fixed distances

1. Localization uncertainty

Almost all BNS sources simulated at the chosen fixed distances were observed with network SN ratio greater than eight. In Table II, we list the percentage of the detectable sources which can be localized to within 30 deg^2, 10 deg^2, 5 deg^2, and 1 deg^2 with each detector network.

All simulated BNS signals at 40 Mpc are detectable to all simulated detector networks and can be localized to an area smaller than 1 deg^2 and are, thus, not shown in Table II. We also note that all sources at 200 Mpc are localized to within 1 deg^2 by all networks. As expected, the localization uncertainty increases with distance increases. Less than 10% sources at 1600 Mpc could be detected within 1 deg^2 by the 3ET network and 2ET1CE networks, while 1ET2CE and 3CE can localize, respectively, 16% and 40% sources.

The cumulative distribution of the size of the 90% credible regions for the BNS mergers at fixed distances are presented in Fig. 3. Results for 200 and 1600 Mpc are shown as an example for simplicity here and results of other fixed distances are presented in the Appendix. We note that the relative behavior of the four networks remain largely unchanged for sources at 200 and 1600 Mpc. Taking 200 Mpc as an example, there is a trend of gradual change

TABLE II. A table showing the fraction of detectable sources which can be localized to within 30 deg^2, 10 deg^2, 5 deg^2 and 1 deg^2 with the GW networks.

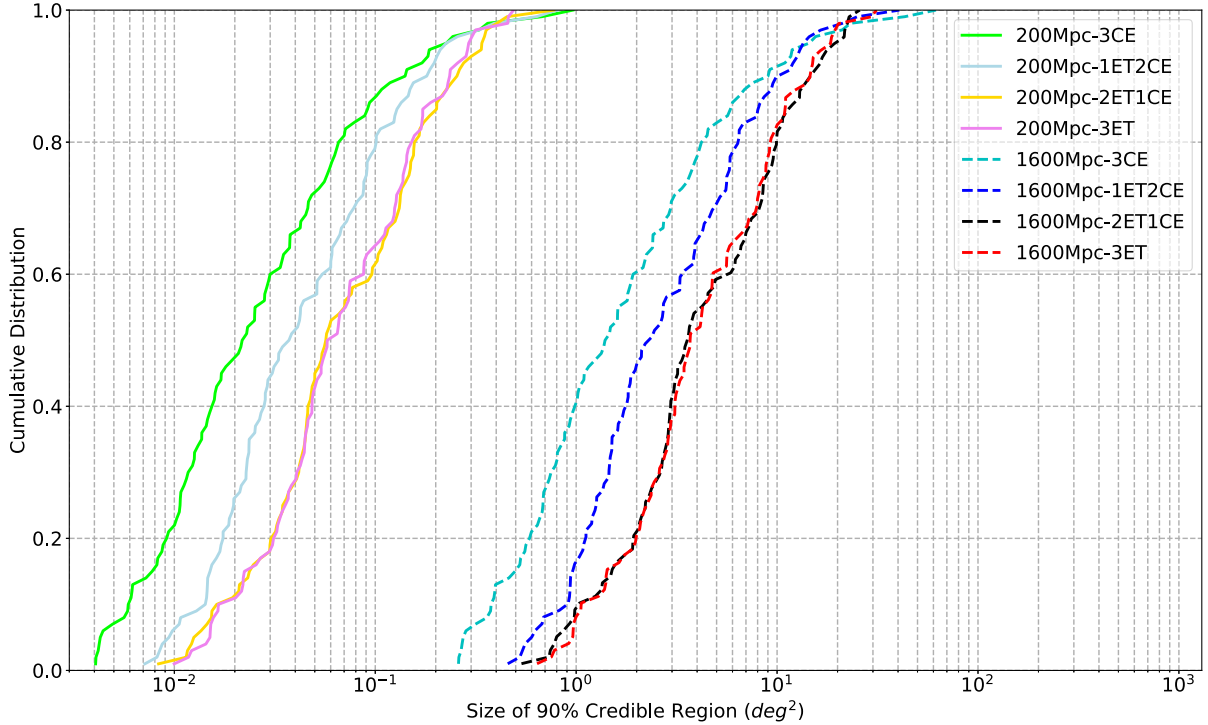| (Mpc)	(deg^2)	3ET (%)	2ET1CE (%)	1ET2CE (%)	3CE (%)
200	30	100	100	100	100
	10	100	100	100	100
	5	100	100	100	100
	1	100	100	100	100
400	30	100	100	100	100
	10	100	100	100	100
	5	100	100	100	100
	1	91	89	95	96
800	30	100	100	100	100
	10	100	99	98	98
	5	95	93	96	96
	1	50	53	64	77
1600	30	99	99	98	98
	10	80	79	89	91
	5	59	58	70	82
	1	7	9	16	40

FIG. 3.　The cumulative distributions of the size of the 90% credible regions for the BNS mergers at 200 and at 1600 Mpc. The *x*-axes show the size of the 90% credible region and the upper limit of the *x*-axes corresponds to the size of the whole sky.

from 3CE to 1ET2CE to 2ET1CE network which gradually accumulate more higher values of localization uncertainty. Additionally, the cumulative distribution of 3ET network is very similar to that of 2ET1CE network.

In Table III, we present the upper limits of the size of the 90% credible regions for the 90%, 50%, and 10% best localized sources. Particularly, 90% of the best localized

TABLE III.　The 90% credible regions of localization uncertainty of every detector network for binary neutron star mergers respectively at 200, 400, 800, and 1600 Mpc with SN ratio > 8. 90%, 50%, and 10% respectively represents the best localized 100%, 90%, and 50% of the detectable sources.

(Mpc)	(%)	3ET (deg^2)	2ET1CE (deg^2)	1ET2CE (deg^2)	3CE (deg^2)
200	90	0.23	0.25	0.18	0.14
	50	0.06	0.06	0.04	0.02
	10	0.02	0.02	0.01	0.01
400	90	0.94	1.02	0.72	0.56
	50	0.23	0.22	0.15	0.09
	10	0.07	0.06	0.06	0.02
800	90	3.75	4.07	2.89	2.25
	50	0.93	0.91	0.60	0.35
	10	0.26	0.26	0.23	0.09
1600	90	14.58	14.65	10.07	9.01
	50	3.69	3.57	2.30	1.39
	10	1.06	1.03	0.90	0.38

sources at 200 Mpc can be constrained to within an area of ~0.3 deg^2 with all four networks. Even for sources at a distance equal to 1600 Mpc, the size of the 90% credible region is still smaller than 15 deg^2, indicating a promising prospect for EM follow-up observations. Furthermore, 50% of the best localized sources respectively at 200, 400, 800, and 1600 Mpc, could be limited to within 0.07 deg^2, 0.30 deg^2, 1.00 deg^2, 4.00 deg^2 by all GW networks. We also found that the localization uncertainty achieved by 2ET1CE for 90% best localized sources at any individual distance is ~1.4 times of that of 1ET2CE network. And it becomes ~1.5 times for 50% best localized sources. For 10% best localized sources, the ratio ranges from 1 to 1.18. Overall, as shown in this table, 2ET1CE network has localization uncertainty no less than 1ET2CE network for simulated sources at fixed distances.

2. Early warning capabilities

As mentioned in Sec. III, the in-band duration of the GW signals from BNS mergers have been significantly extended for third generation detectors. It is therefore possible for a signal to accumulate enough SNR to be deemed significant before the merger. This in turn makes it possible that a trigger may be released prior to merger, increasing the likelihood of a successful EM follow-up observation.

To evaluate the early warning prospect of the simulated networks of GW detectors, we require two conditions
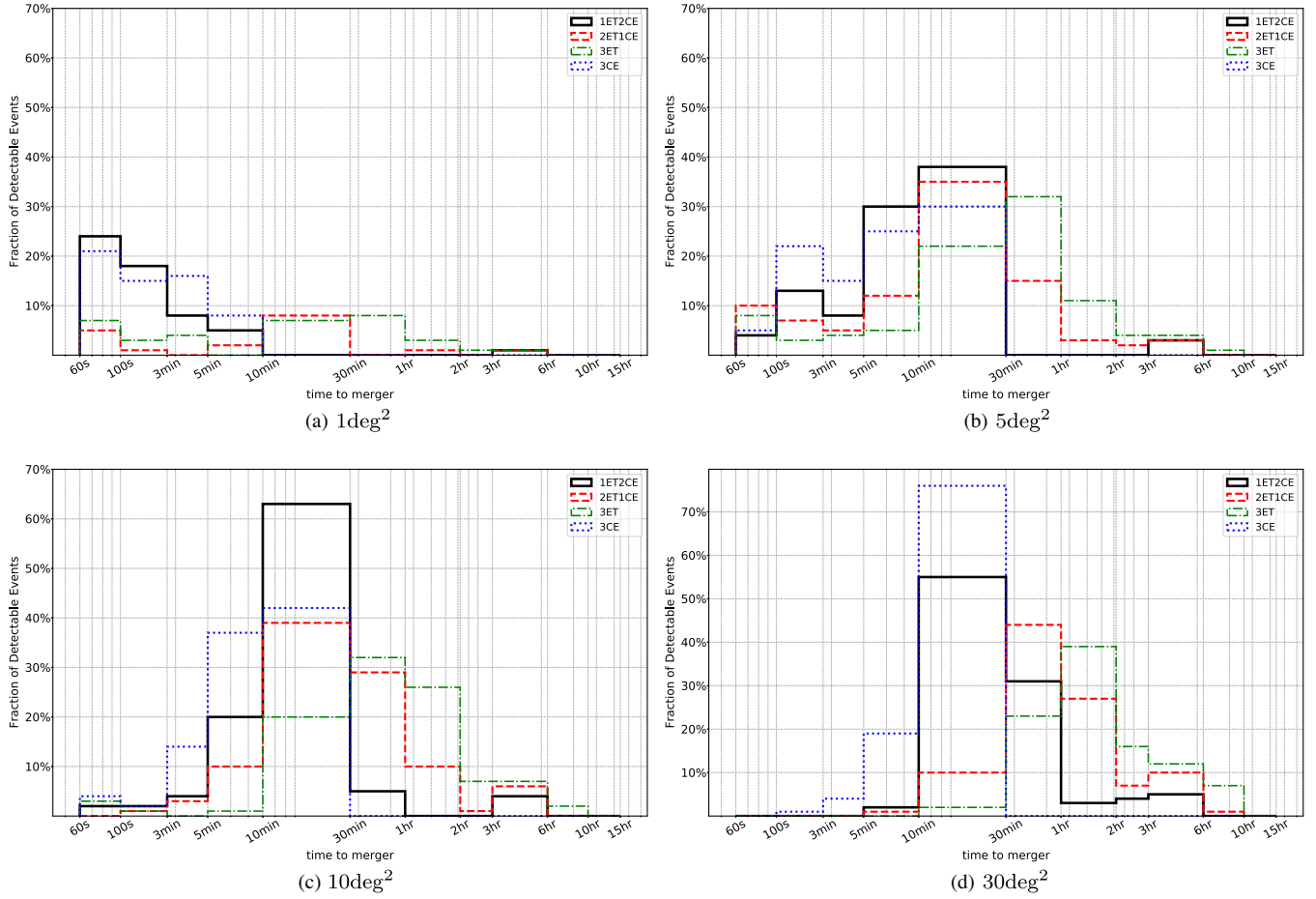
(a) 1deg^2

(b) 5deg^2

(c) 10deg^2

(d) 30deg^2

FIG. 4.   Histograms showing the distributions of time to merger for the BNS mergers at 200 Mpc with four detector networks. The *x*-axis is the time to merger when the signal meets the early warning criteria. The *y*-axis is the fraction of detectable events that achieve these early warning criteria. The percentage of sources that could be detected within required localization uncertainty could be found in Table II.

to be satisfied before a trigger can be released. The first condition is that the signal has to accumulate a network SNR of no less than 8 at the time the trigger is released, and the other condition is that the source of the signal has to be localized to an error no greater than a given certain area with 90% confidence. The second condition is required because a signal may accumulate enough SN ratio to the point where the event is considered significant prior to merger, but the localization error is still too large for any meaningful EM follow-up observations to be carried out. These two conditions will be referred to as early warning criteria in the remaining of this paper. Furthermore, in terms of the second condition of early warning, we chose localization area of respectively 30 deg^2, 10 deg^2, 5 deg^2 and 1 deg^2 as requirements to evaluate corresponding time to merger distribution under these conditions.

Figure 4 presents the histogram distribution of time to merger of four detector network for BNSs at 200 Mpc, where each subplot denotes the time to merger distribution given maximum allowable localization uncertainty of,

respectively, 30 deg^2, 10 deg^2, 5 deg^2, and 1 deg^2. It should be noted that the sum of percentages for each network may not be 100% because there are some sources
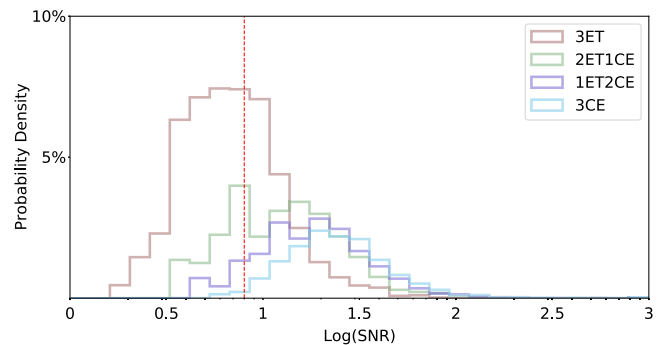

FIG. 5.   The probability density distributions of the SN ratio for the BNS which follow the DTD. The horizontal axis represents the SN ratio in log scale. The network combined SN ratio threshold of 8 is denoted by a red dashed vertical line. The area under the histogram is normalized to be 1.

TABLE IV. A table showing the upper limits for the size of the 90% credible regions for the best localized 90%, 50%, and 10% of the detectable sources following DTD. The second row denotes the percentage of the detectable sources for the detector networks.

	3ET (deg^2)	2ET1CE (deg^2)	1ET2CE (deg^2)	3CE (deg^2)
	63.0%	89.8%	97%	99.4%
90%	31.59	91.79	56.77	44.68
50%	10.25	17.57	12.54	7.02
10%	0.97	1.37	1.17	0.61

which could be detected within the required localization uncertainty only at the time of merger. Early warning of BNSs at 200 Mpc will be discussed in detail here, the related figures of BNSs at other fixed distances could be found in the Appendix.

Given the maximum localization uncertainty of 30 deg^2, 100% BNS signals at 200 Mpc could be detected by all tested GW detector networks at least 100 seconds before merger. The time to merger of BNSs detected by 1ET2CE network ranges from five minutes to six hours, and is concentrated in range of ten minutes to one hour. While for 2ET1CE network, it ranges from five minutes to ten hours, and is mainly distributed between ten minutes and six hours. The range of time to merger indicates a significant possibility of third generation GW detector networks to give early warning alert to EM follow-up observations.

When the maximum allowable localization uncertainty decreases to 10 deg^2, 5 deg^2, and 1 deg^2—detectable sources which meet the early warning criteria become less and less—part of BNS signals could only meet the early warning criteria at the time of merger, and the distribution of time to merger move towards to a direction of smaller value. We found that given the same maximum allowable localization uncertainty and network SN ratio threshold, comparing to 1ET2CE network, signals observed by 2ET1CE network are more likely to meet the early warning criteria at an earlier time prior to merger, thus presenting a more promising prospect for early warning.

B. Astrophysical population

1. Signal-to-noise ratio distributions

For the BNS mergers following the DTD, the SN ratio distribution is presented in Fig. 5. In total, there are 63.0%, 89.8%, 97%, and 99.4% BNS mergers detectable to 3ET, 2ET1CE, 1ET2CE, and 3CE, respectively, as listed in Table IV. For networks consisting of more CE-like detectors such as 1ET2CE and 3CE, the distribution of SN ratios peak at higher values, which is largely due to the better sensitivity of CE at higher frequencies.

2. Localization uncertainty

For all simulated BNS sources following the DTD, all detector networks can localize BNS signals within
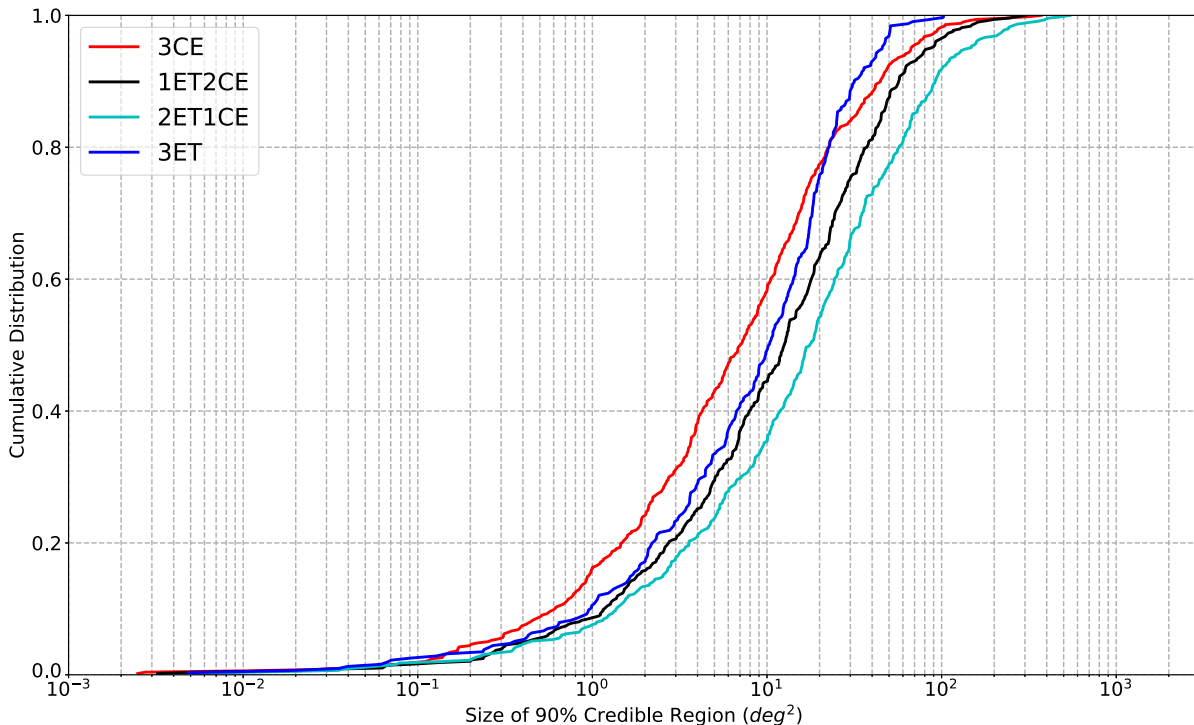

FIG. 6. The cumulative distribution of the size of the 90% credible region for the BNS mergers following the DTD. The *x*-axis show the size of 90% credible region in deg^2.

$\mathcal{O}(10^2)$ deg^2. The cumulative distribution of size of the 90% credible regions are shown in Fig. 6. It should be noted that only localization results of those detectable sources as described in Sec. IV B 1 are presented in Fig. 6. As we can see, the curve of 2ET1CE, 1ET2CE, and 3CE have a trend of gradual change, toward a direction of occupying more proportion at smaller values of localization uncertainty. Behavior of 3ET is deviated from prediction of this gradual change, which originates from detectable source selection effect. The upper limits of the localization errors for the 90%, 50%, and 10% best localized sources are shown in Table IV. It could be found from Table IV that for best localized 90% detectable sources, the 2ET1CE network could localize sources within 91.79 deg^2, and maximum localization uncertainty of the 1ET2CE network shrinks by about 0.38 times compared to that of the 2ET1CE network. In addition, the 1ET2CE network could localize best localized half of detectable sources within 12.54 deg^2, which is about 0.28 times smaller than 17.57 deg^2 of the

2ET1CE network. For the best localized 10% of detectable sources, the differences are smaller, but the trend remains the same, 1ET2CE could localize sources within 1.17 deg^2 which is still less than 1.37 deg^2 of the 2ET1CE network.

3. Early warning capabilities

The results are presented in Fig. 7 as a two-dimensional histogram showing the distribution of time to merger versus the size of 90% credible region for BNS mergers following DTD. The chosen value of 30 deg^2 is motivated by the fact that all simulated events at 1600 Mpc can be localized to within such an area with all simulated networks. For comparison, we also employ 100 deg^2 as the value for the second condition. The result is shown in the Appendix.

From Fig. 7, the 3ET network and the 2ET1CE network could both detect several BNS signals more than ten hours before merger with a localization uncertainty smaller than 30 deg^2. In terms of the detectable source quantity, more
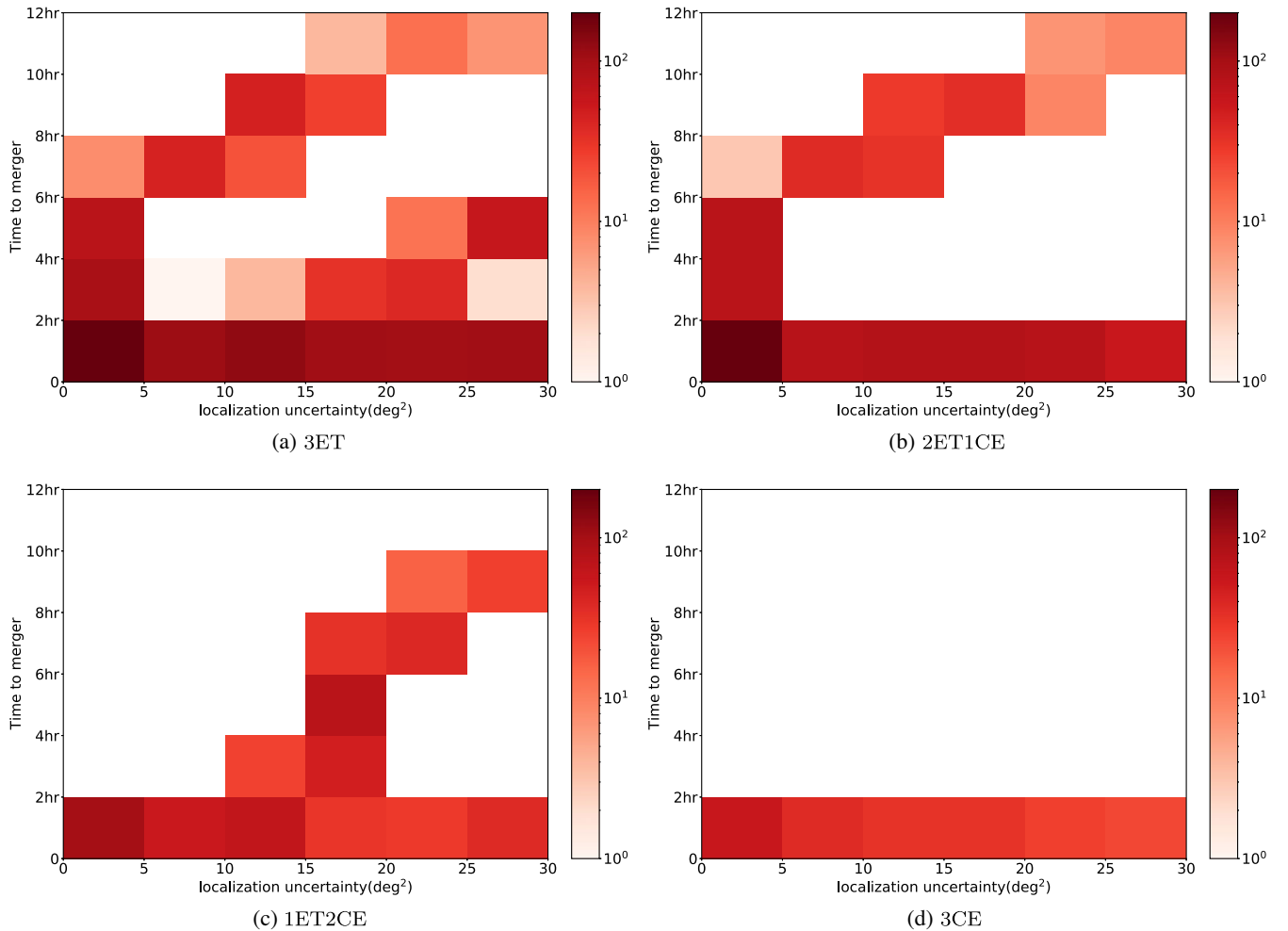

FIG. 7. Two-dimensional histograms showing the distributions of the time to merger for BNS mergers following DTD. The horizontal axis of every subplot is the size of the 90% credible region, and the vertical axis represents the time to merger. The color represents the number of sources which achieve the early warning criteria with the localization requirement being ≤30 deg^2.

CE included networks could detect more sources which achieve the early warning criteria, but in terms of the time to merger distribution, it is obvious that early warning of more ET included networks are more widely distributed and peaked at higher values in the vertical direction. For example, for the 1ET2CE network, which replaces one CE with ET in the 3CE network, the upper right corner of the figure fills in the blanks, which means joining of ET improves the early warning performance to some extent, and could give an early warning alert as early as ten hours. Besides, compared to the 1ET2CE network, the 2ET1CE network could still detect some signals as early as ten hours with smaller localization uncertainty, which indicates a greater opportunity to perform successful EM follow-up observations.

V. CONCLUSION AND DISCUSSION

GW detections are rapidly evolving as a routine tool in the multimessenger era. Maximizing GW's scientific output by associating with its EM counterpart is our major goal in multimessenger astronomy. Localization and early warning performance of a GW detector largely affects the efficiency of EM follow-up operations. In this paper, we calculated and compared the localization uncertainty and early warning performance of four third generation ground-based GW detector networks for BNS sources at fixed distance and BNS sources following DTD. The duration of simulated signals is about five days long; therefore, we included the Earth's rotation effect, and considering that the detector moves relative to the source we also included the Doppler effect. Besides the ET to be built in Europe, and the CE to be built in North America, we also simulated four detector networks involving combinations of the aforementioned detectors and the following: ET in Australia (ET-A), CE in Australia (CE-A), ET in North America, and CE in Italy. The comparison of localization capabilities of ET-A included network and CE-A included network is especially important.

In terms of the SN ratio for a BNS population following the DTD approach, networks with more CE detectors tend to have higher SN ratios due to the CE having better sensitivity at the medium to high frequency band, leading to a smaller source localization uncertainty. Using Fisher matrix analysis, 90% of the best localized sources can be localized within an area of respectively 31.59 $\deg^2$, 91.79 $\deg^2$, 56.77 $\deg^2$, and 44.68 $\deg^2$ for the 3ET, 2ET1CE, 1ET2CE, and 3CE network. The 3ET network seems to give an excellent source localization estimate but only because poorly localized sources are rejected due to their SN ratio not being above the required threshold of 8. For BNS mergers at fixed distances, the comparison of localization performance between tested networks remain similar to that of BNS mergers following DTD.

In terms of time to merger distribution, for BNSs at 200 Mpc, all tested networks achieved the early warning criteria of 30 $\deg^2$ at least 100 seconds before merger. The time to merger distribution is widely distributed in range of 100 seconds to 10 hours, which indicates a bright future for successful EM follow-up observations in the third generation GW detector era. For both BNS mergers at fixed distances and following DTD, more ET included networks are more likely to detect BNS signals earlier because the better sensitivity of ET in low-frequency band, leading to BNS signals being in-band for longer.

Overall, compared with the 2ET1CE network, the 1ET2CE network detects more BNS signals while achieving a better localization uncertainty. However, the 2ET1CE network tends to give alerts earlier than the 1ET2CE network. All things considered, we think building a CE-like detector in Australia to create the 1ET2CE network is a reasonable compromise, as this would lead to an excellent localization performance without losing too much early warning performance compared to 2ET1CE network.

APPENDIX: ADDITIONAL RESULTS

The cumulative distribution of localization uncertainty for BNS mergers at 40, 400, and 800 Mpc are shown in Fig. 8. In addition, Fig. 9, Fig. 10, Fig. 11, and Fig. 12 are the histogram distribution of time to merger respectively for BNS mergers at 40, 400, 800, and 1600 Mpc. Finally, Fig. 13 show the two-dimensional histograms distributions of the time to merger for BNS mergers following DTD with maximum allowable region of 100 $\deg^2$.
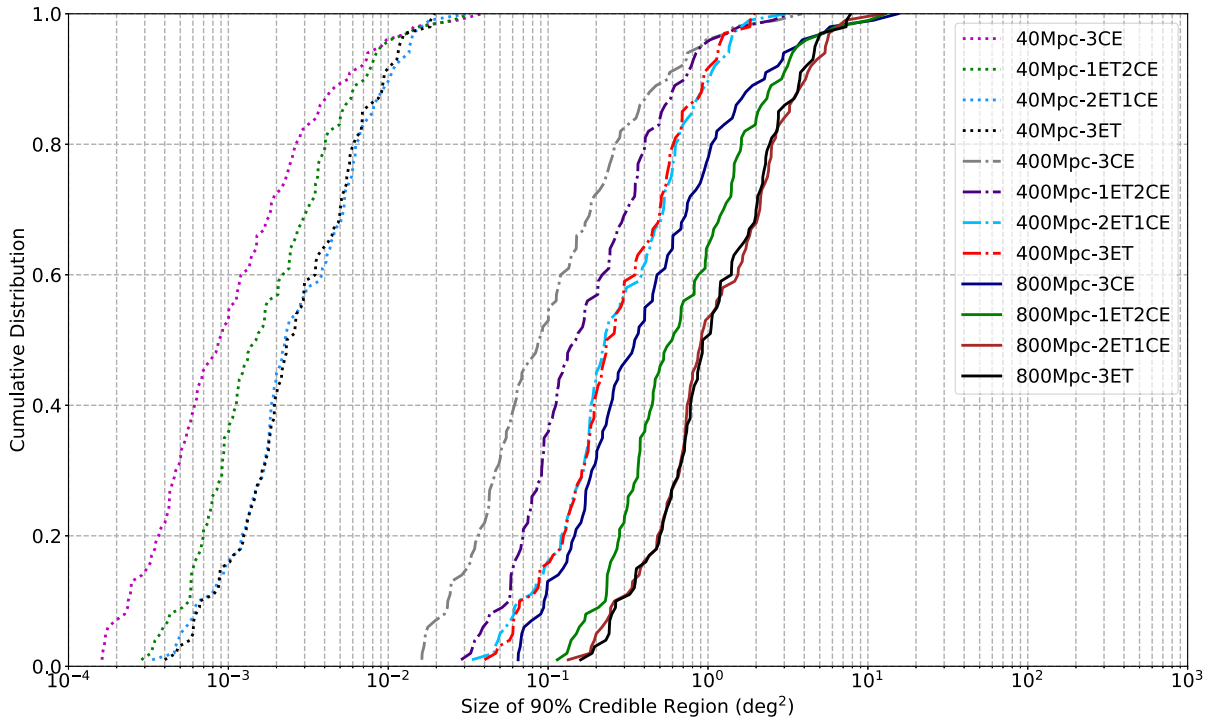
FIG. 8. The cumulative distributions of the size of the 90% credible regions for the BNS mergers at 40, 400, and at 800 Mpc. The x-axes show the size of the 90% credible region and the upper limit of the x-axes corresponds to the size of the whole sky.
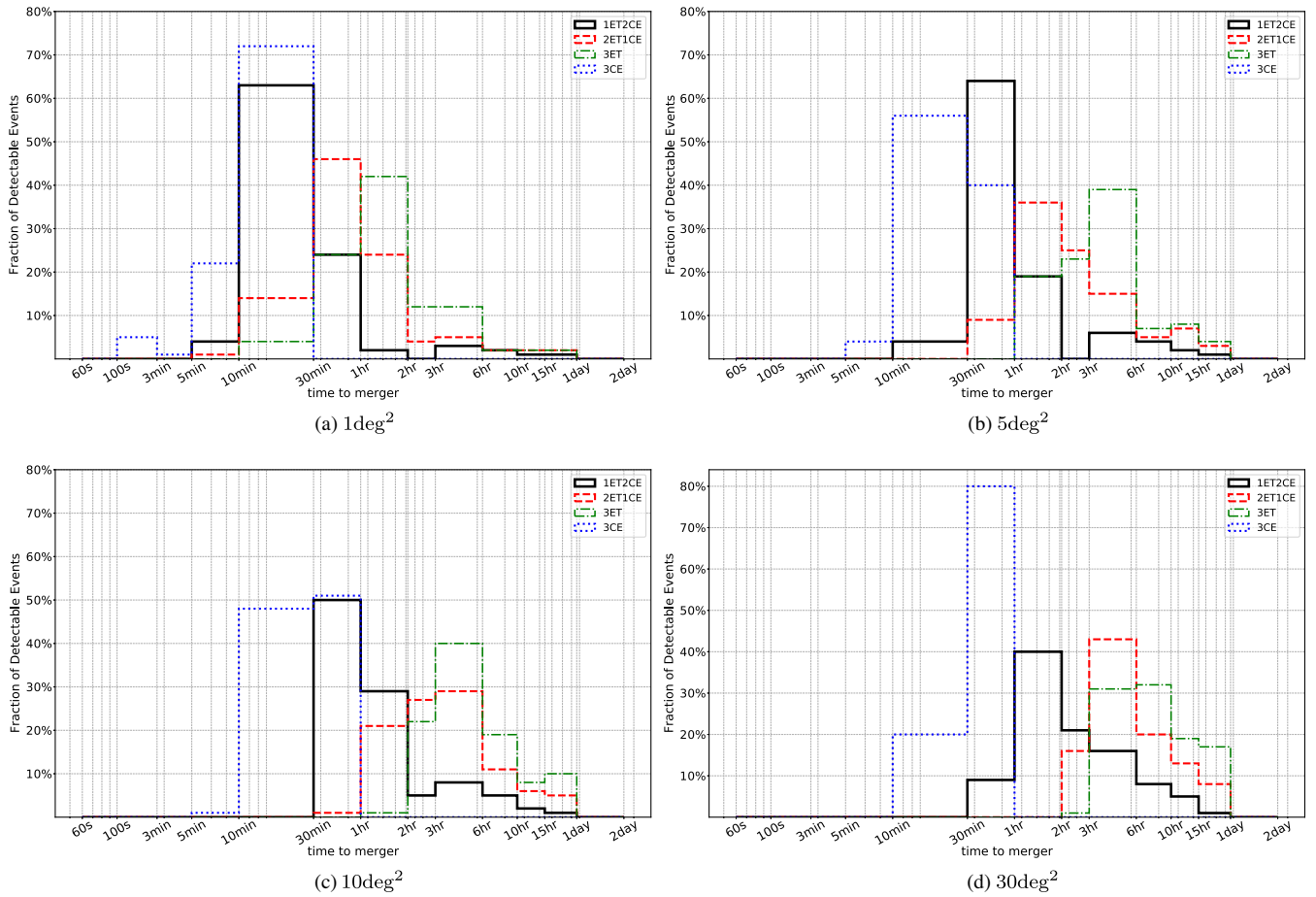

FIG. 9. The histogram distribution of time to merger by 4 detector networks for BNS at 40 Mpc with required localization uncertainty denoted as caption of each subplot.
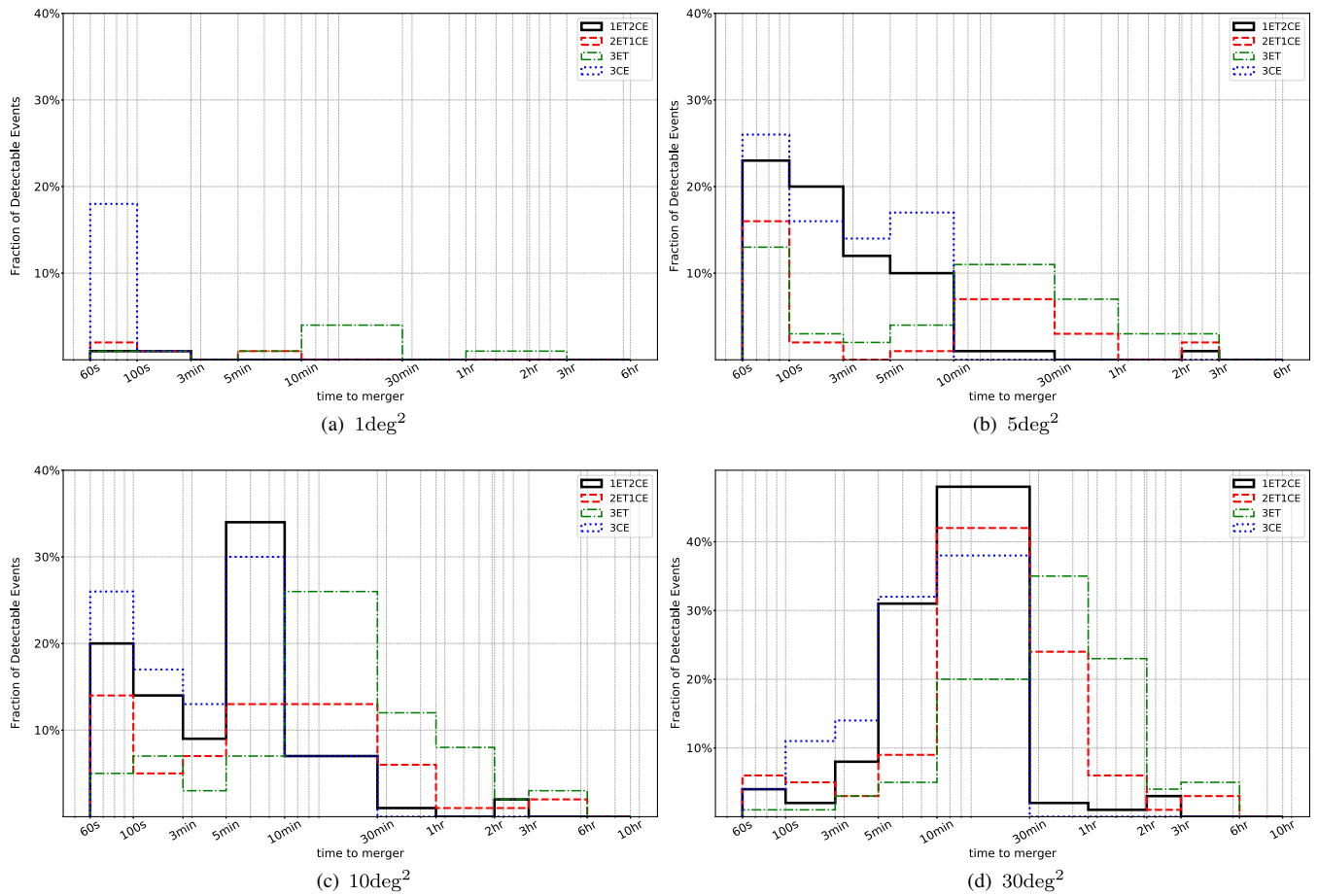
FIG. 10. The histogram distribution of time to merger by four detector networks for BNS at 400 Mpc with required localization uncertainty denoted as caption of each subplot.
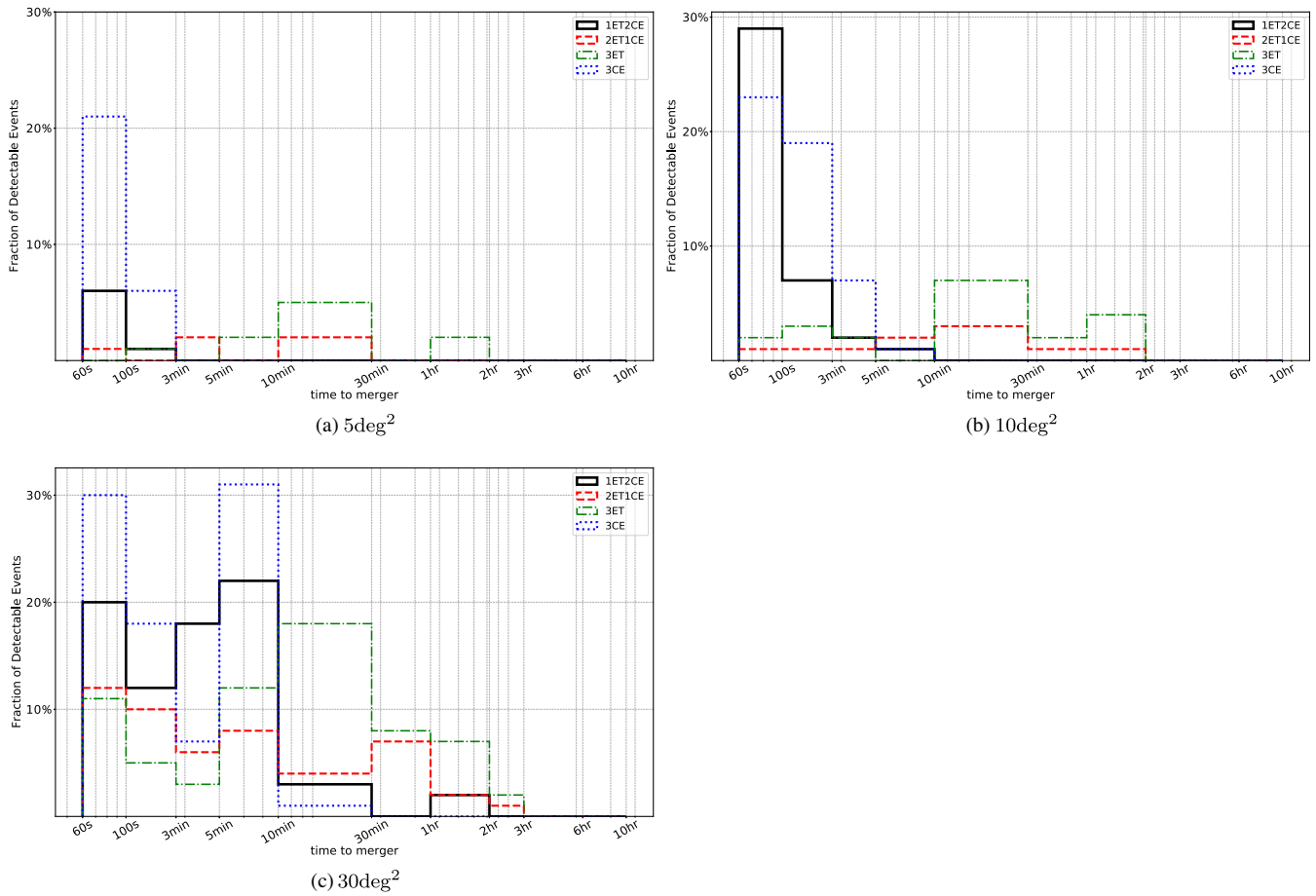
FIG. 11. The histogram distribution of time to merger by 4 detector networks for BNS at 800 Mpc with required localization uncertainty denoted as caption of each subplot.
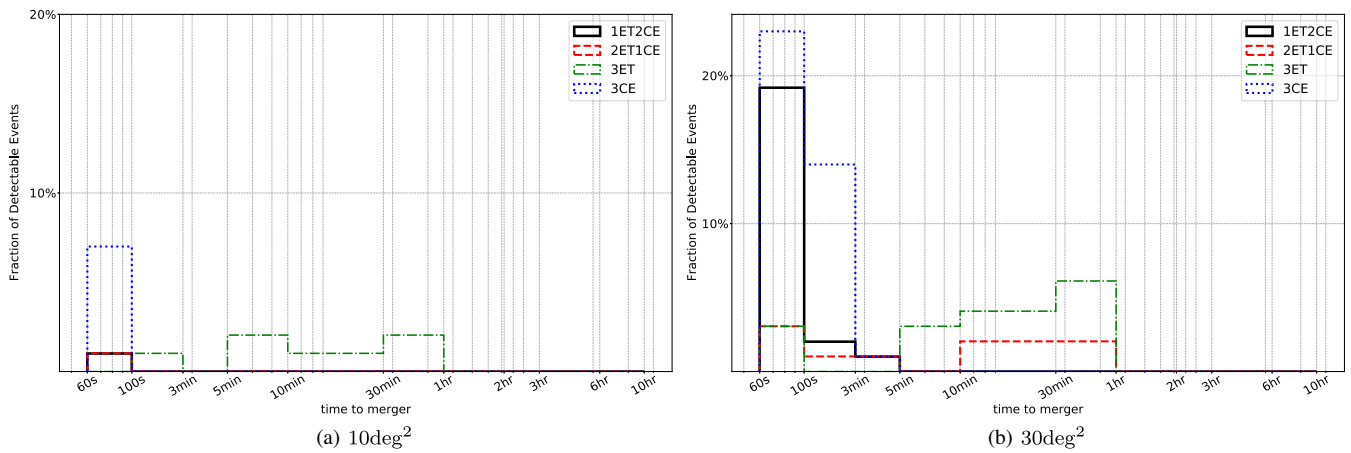

FIG. 12. The histogram distribution of time to merger by four detector networks for BNS at 1600 Mpc with required localization uncertainty denoted as caption of each subplot.
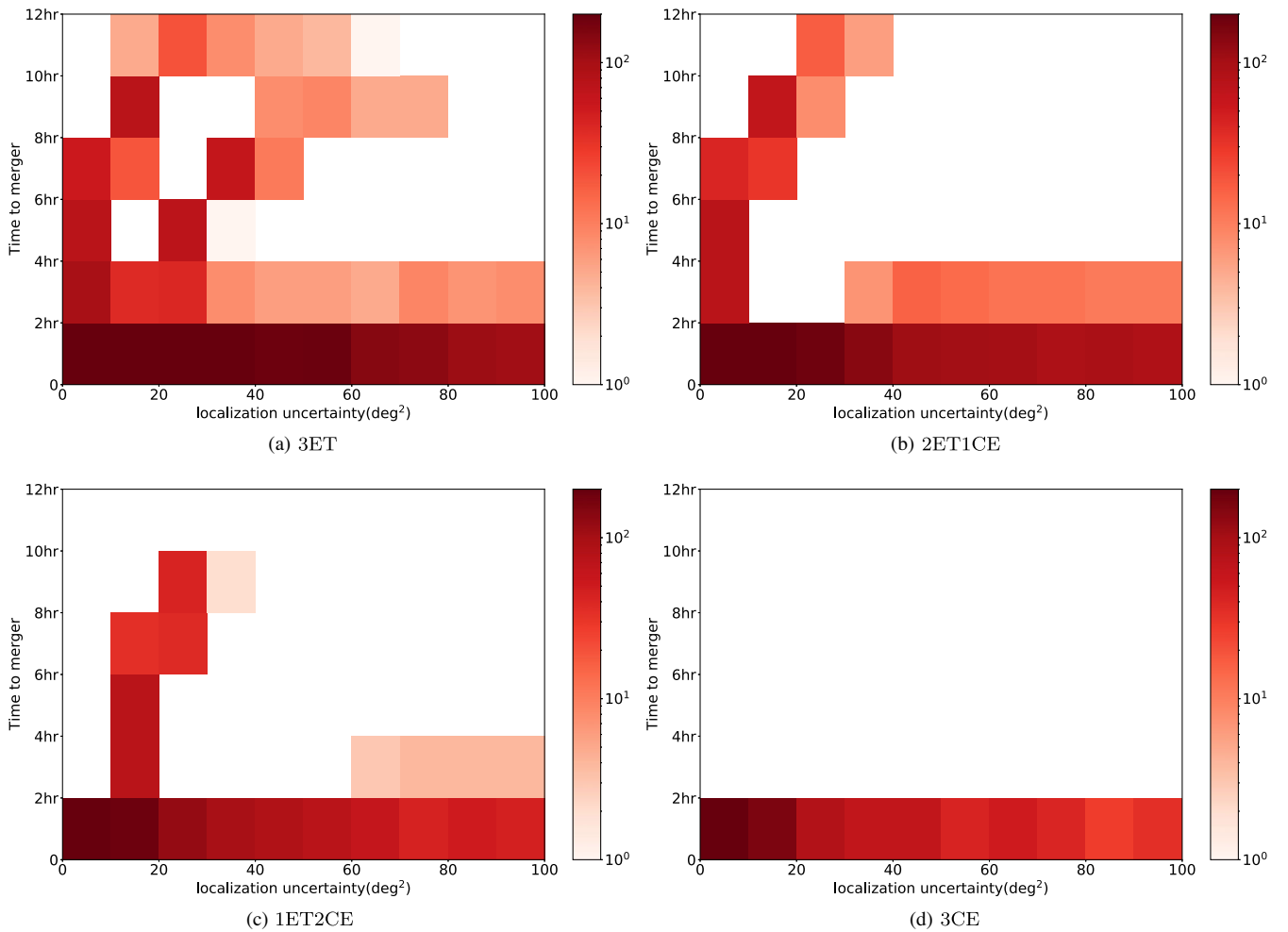
FIG. 13. Two-dimensional histograms showing the distributions of the time to merger for BNS mergers following DTD. The horizontal axis of every subplot is the size of the 90% credible region, and the vertical axis represents the time to merger. The color represents the number of sources which achieve the early warning criteria with the localization requirement being $\leq 100 \ \mathrm{deg}^2$.

[1] B. P. Abbott *et al.*, Observation of Gravitational Waves from a Binary Black Hole Merger, Phys. Rev. Lett. **116,** 061102 (2016).

[2] F. Acernese, M. Agathos, K. Agatsuma *et al.*, Advanced Virgo: A second-generation interferometric gravitational wave detector, Classical Quantum Gravity **32,** 024001 (2015).

[3] B. P. Abbott, R. Abbott, T. D. Abbott *et al.*, GWTC-1: A Gravitational-Wave Transient Catalog of Compact Binary Mergers Observed by LIGO and Virgo during the First and Second Observing Runs, Phys. Rev. X **9,** 031040 (2019).

[4] B. P. Abbott, R. Abbott, T. D. Abbott *et al.*, GW170817: Observation of Gravitational Waves from a Binary Neutron Star Inspiral, Phys. Rev. Lett. **119,** 161101 (2017).

[5] R. Abbott, T. D. Abbott, S. Abraham *et al.*, GWTC-2: Compact Binary Coalescences Observed by LIGO and

[6] R. Abbott *et al.* (The LIGO Scientific Collaboration, the Virgo Collaboration), GWTC-2.1: Deep extended catalog of compact binary coalescences observed by LIGO and Virgo during the first half of the third observing run, arXiv:2108.01045.

[7] R. Abbott, T. D. Abbott, S. Abraham *et al.*, Population properties of compact objects from the second LIGO–Virgo gravitational-wave transient catalog, Astrophys. J. Lett. **913,** L7 (2021).

[8] M. Safarzadeh and E. Berger, Measuring the delay time distribution of binary neutron stars. I. Through scaling relations of the host galaxies of gravitational-wave events, Astrophys. J. Lett. **878,** L12 (2019).

[9] M. Safarzadeh, E. Berger, K. K. Y. Ng *et al.*, Measuring the delay time distribution of binary neutron stars. II. Using the

Virgo during the First Half of the Third Observing Run, Phys. Rev. X **11,** 021053 (2021).

redshift distribution from third-generation gravitational-wave detectors network, Astrophys. J. Lett. **878**, L13 (2019).

[10] M. Safarzadeh, E. Berger, J. Leja, and J. S. Speagle, Measuring the delay time distribution of binary neutron stars. III. Using the individual star formation histories of gravitational-wave event host galaxies in the local universe, Astrophys. J. Lett. **878**, L14 (2019).

[11] I. Hachisu, M. Kato, and K. Nomoto, The delay-time distribution of type Ia supernovae and the single-degenerate model, Astrophys. J. Lett. **683**, L127 (2008).

[12] T. Piran, The implications of the compton (GRO) observations for cosmological gamma-ray bursts, Astrophys. J. Lett. **389**, L45 (1992).

[13] Z. Zheng and E. Ramirez-Ruiz, Deducing the lifetime of short gamma-ray burst progenitors from host galaxy demography, Astrophys. J. **665**, 1220 (2007).

[14] B. D. Metzger and E. Berger, What is the most promising electromagnetic counterpart of a neutron star binary merger?, Astrophys. J. **746**, 48 (2012).

[15] B. D. Metzger, G. Martínez-Pinedo, S. Darbha, E. Quataert, A. Arcones, D. Kasen, R. Thomas, P. Nugent, I. V. Panov, and N. T. Zinner, Electromagnetic counterparts of compact object mergers powered by the radioactive decay of r-process nuclei, Mon. Not. R. Astron. Soc. **406**, 2650 (2010).

[16] A. Hajela, R. Margutti, K. D. Alexander et al., Two years of nonthermal emission from the binary neutron star merger GW170817: Rapid fading of the jet afterglow and first constraints on the kilonova fastest ejecta, Astrophys. J. Lett. **886**, L17 (2019).

[17] B. P. Abbott, R. Abbott, T. D. Abbott et al., On the progenitor of binary neutron star merger GW170817, Astrophys. J. Lett. **850**, L40 (2017).

[18] M. Branchesi, Multi-messenger astronomy: Gravitational waves, neutrinos, photons, and cosmic rays, J. Phys. Conf. Ser. **718**, 022004 (2016).

[19] L. K. Nuttall and P. J. Sutton, Identifying the host galaxy of gravitational wave signals, Phys. Rev. D **82**, 102002 (2010).

[20] B. P. Abbott, R. Abbott, T. D. Abbott et al., A gravitational-wave measurement of the Hubble constant following the second observing run of advanced LIGO and Virgo, Astrophys. J. **909**, 218 (2021).

[21] K. Hotokezaka, E. Nakar, O. Gottlieb, S. Nissanke, K. Masuda, G. Hallinan, K. P. Mooley, and A. T. Deller, A Hubble constant measurement from superluminal motion of the jet in GW170817, Nat. Astron. **3**, 940 (2019).

[22] R. Margutti, P. Cowperthwaite, Z. Doctor et al., Target of opportunity observations of gravitational wave events with LSST, arXiv:1812.04051.

[23] K. Cannon, R. Cariou, A. Chapman et al., Toward early-warning detection of gravitational waves from compact binary coalescence, Astrophys. J. **748**, 136 (2012).

[24] M. Punturo, H. Lück, and M. Beker, A third generation gravitational wave observatory: The Einstein Telescope, in *Advanced Interferometers and the Search for Gravitational Waves* (Springer, Cham, 2014), pp. 333–362, 10.1007/978-3-319-03792-9_13.

[25] B. P. Abbott, R. Abbott, T. D. Abbott et al., Exploring the sensitivity of next generation gravitational wave detectors, Classical Quantum Gravity **34**, 044001 (2017), https://ui .adsabs.harvard.edu/abs/2017CQGra..34d4001A/abstract.

[26] S. Akcay, Forecasting gamma-ray bursts using gravitational waves, Ann. Phys. (Berlin) **531**, 1 (2018).

[27] S. Akcay, M. Fraser, and A. Martin-Carrillo, A crystal ball for kilonovae, arXiv:1812.07307.

[28] M. L. Chan, C. Messenger, I. S. Heng, and M. Hendry, Binary neutron star mergers and third generation detectors: Localization and early warning, Phys. Rev. D **97**, 123014 (2018).

[29] C. Mills, V. Tiwari, and S. Fairhurst, Localization of binary neutron star mergers with second and third generation gravitational-wave detectors, Phys. Rev. D **97**, 104064 (2018).

[30] W. Zhao and L. Wen, Localization accuracy of compact binary coalescences detected by the third-generation gravitational-wave detectors and implication for cosmology, Phys. Rev. D **97**, 064031 (2018).

[31] P. Barriga, D. G. Blair, D. Coward et al., AIGO: A southern hemisphere detector for the worldwide array of ground-based interferometric gravitational wave detectors, Classical Quantum Gravity **27**, 084005 (2010).

[32] E. J. Howell, M. L. Chan, Q. Chu et al., Host galaxy identification for binary black hole mergers with long baseline gravitational wave detectors, Mon. Not. R. Astron. Soc. **474**, 4385 (2018).

[33] S. Nissanke, J. Sievers, N. Dalal, and D. Holz, Localizing compact binary inspirals on the sky using ground-based gravitational wave interferometers, Astrophys. J. **739**, 99 (2011).

[34] M. Punturo, M. Abernathy, F. Acernese et al., The Einstein Telescope: A third-generation gravitational wave observatory, Classical Quantum Gravity **27**, 194002 (2010).

[35] S. Dwyer, D. Sigg, S. W. Ballmer, and M. Evans, Gravitational wave detector with cosmological reach, Phys. Rev. D **91**, 082001 (2015).

[36] D. Reitze et al., Cosmic explorer: The U.S. contribution to gravitational-wave astronomy beyond LIGO, Bull. Am. Astron. Soc. **51**, 141 (2019), https://ui.adsabs.harvard .edu/abs/2019BAAS...51g..35R/abstract.

[37] W. Zhao, Gravitational-wave standard siren and cosmology, Sci. Sin. Phys. Mech. Astron. **48**, 079805 (2018).

[38] T. Regimbau, T. Dent, W. Del Pozzo, S. Giampanis, T. G. F. Li, C. Robinson, C. Van Den Broeck, D. Meacher, C. Rodriguez, B. S. Sathyaprakash, and K. Wójcik, Mock data challenge for the Einstein Gravitational-Wave Telescope, Phys. Rev. D **86**, 122001 (2012).

[39] B. F. Schutz, Networks of gravitational wave detectors and three figures of merit, Classical Quantum Gravity **28**, 125023 (2011).

[40] J. Abadie, B. P. Abbott, R. Abbott et al., Search for gravitational waves from binary black hole inspiral, merger, and ringdown, Phys. Rev. D **86**, 069903 (2012).

[41] A. Buonanno, B. R. Iyer, E. Ochsner, Y. Pan, and B. S. Sathyaprakash, Comparison of post-Newtonian templates for compact binary inspiral signals in gravitational-wave detectors, Phys. Rev. D **80**, 084043 (2009).

[42] M. Maggiore, *Gravitational Waves. Vol. 1: Theory and Experiments* (Oxford University Press, Oxford, England, 2007).

[43] P. A. R. Ade, N. Aghanim *et al.* (Planck Collaboration), Planck 2015 results XIII. Cosmological parameters, Astron. Astrophys. **594**, A13 (2016).

[44] P. Madau and M. Dickinson, Cosmic star-formation history, Annu. Rev. Astron. Astrophys. **52**, 415 (2014).

[45] B. A. Bassett, Y. Fantaye, R. Hlozek, and J. Kotze, Fisher matrix preloaded—fisher4cast, Int. J. Mod. Phys. D **20**, 2559 (2011).

[46] S. Fairhurst, Triangulation of gravitational wave sources with a network of detectors, New J. Phys. **11**, 123006 (2009).

[47] S. Fairhurst, Source localization with an advanced gravitational wave detector network, Classical Quantum Gravity **28**, 105021 (2011).

[48] L. Wen and Y. Chen, Geometrical expression for the angular resolution of a network of gravitational-wave detectors, Phys. Rev. D **81**, 082001 (2010).

[49] M. Vallisneri, Use and abuse of the Fisher information matrix in the assessment of gravitational-wave parameter-estimation prospects, Phys. Rev. D **77**, 042001 (2008).

[50] C. P. L. Berry, I. Mandel, H. Middleton *et al.*, Parameter estimation for binary neutron-star coalescences with realistic noise during the advanced LIGO era, Astrophys. J. **804**, 114 (2015).

[51] Bin Wang, Wenzhong Shi, and Zelang Miao, Confidence analysis of standard deviational ellipse and its extension into higher dimensional euclidean space, PLoS One **10**, 1 (2015).